Single-Laser Krypton Tagging Velocimetry Investigation of Supersonic Air and N_{2} Boundary-Layer Flows over a Hollow Cylinder in a Shock Tube

Muhammad A. Mustafa, David Shekhtman, and Nick J. Parziale

Single-Laser Krypton Tagging Velocimetry (KTV) Investigation of Supersonic Air and N₂ Boundary-Layer Flows Over a Hollow Cylinder in a Shock Tube

Muhammad A. Mustafa, David Shekhtman, and Nick J. Parziale*
Stevens Institute of Technology,
Mechanical Engineering, Castle Point on Hudson,
Hoboken, New Jersey, 07030.

In this paper, we investigate the boundary-layer profiles that form over a sharp, hollow cylinder in supersonic air and N₂ flows with a Krypton Tagging Velocimetry (KTV) single-laser scheme. The supersonic flows are generated by the passage of the primary shock wave over the model in the Stevens Shock Tube. The experiments were performed in two gas mixtures doped with Kr; 99% N₂/1% Kr, to model N₂, and 75% N₂/20% O₂/5% Kr, to model air. The experimental setup allowed us to vary the pressure and Reynolds number from $3 - 25$ kPa and $1.5 \times 10^5 - 1.5 \times 10^6$ m^{-1}, respectively, while the Mach number was kept fixed at 1.7. The static temperature and pressure (but not the velocity) are representative of typical large-scale high-enthalpy hypersonic impulse facilities. The KTV data points over the hollow cylinder are mapped to corresponding wall-normal locations above a flat plate, which enabled comparison with the similarity solution for compressible boundary-layer flow. Agreement between the similarity solution and experimental results is excellent. Relative to previous two-laser KTV schemes, the single-laser approach used in this work has the advantage of being simpler and more cost-effective, but has a higher laser energy requirement, 10 mJ/pulse in these experiments. Single-laser KTV is implemented by increasing the energy of the write-laser pulse to a sufficient level such that the Kr becomes partially ionized via a (2+1) resonance-enhanced, multiphoton ionization (REMPI) process with an excitation wavelength of 212.6 nm. The write step records the fluorescence that results primarily from the spontaneous emission from the two-photon excitation. After a prescribed delay, the read step records the fluorescence that results from the transitions that follow the recombination process. The signal-to-noise-ratio (SNR) is sufficient to extract velocity profiles from single-shot, shock-tube experiments. Two-photon absorption cross-section calculations and emission spectra are presented to justify the chosen excitation wavelength and support our understanding of the Kr excitation/emission scheme.

I. INTRODUCTION

High-speed flow is characterized by various complex phenomena such as shock waves, turbulence, chemical reactions, and non-equilibrium effects. These complex phenomena and their interactions have aerothermodynamic design implications for high-speed vehicles. To optimize the design of such vehicles, it is necessary to generate predictive computational tools that are capable of modeling high-speed flow physics. To this end, non-intrusive, off-surface experimental techniques are required to assess computational-model performance while they are being developed and applied to canonical flows; additionally, advanced diagnostics serve as a check on computational-model performance during the vehicle design stage.

Many variables are of interest when comparing experimental and computational results; velocity is one such variable [1]. Ubiquitous particle-based measurement techniques such as PIV [2, 3], rely on the assumption that the tracer particles travel identically with the flow. However, the particle response time can be inadequate in low-density, high-Mach-number flows with short time scales because of particle slip due to high Knudsen number [4]. This represents a fundamental limitation of particle-based techniques because the slip condition at the particle surface reduces response time. Several researchers [5–7] have examined the response of particles to shock waves in an effort to quantify particle response time. Williams *et al.* [8] suggest that "particle frequency response analyses based solely on shock response tests may well have overestimated the response to turbulence." Measurement of velocity fluctuations in high-speed, turbulent boundary layers is an example that brings the particle-response-time limitation to bear. Lowe *et al.* [9] assert that "[s]trong evidence exists that experimental data gathered in high speed flows using particle-based techniques exhibit significant particle lag effects on magnitudes of turbulence quantities." This assertion was based on an experimental Laser-Doppler Velocimetry (LDV) campaign in a Mach 2.0 turbulent boundary layer, and the authors made particle-lag corrections to address discrepancies in their data. Recent Particle-Image Velocimetry (PIV) work by Brooks *et al.* [10] found that particle-lag effects are more pronounced in the turbulence quantities associated with the wall-normal velocity than the streamwise velocity. This is because the wall-normal velocity fluctuation spectrum is flatter (has more high-frequency content) than its streamwise counterpart.

An attractive alternative to particle-based techniques is tagging velocimetry. Tagging velocimetry [11] is typically performed in gases by tracking the fluorescence of a native, seeded, or synthesized gas. Its advantage

* nick.parziale@gmail.com

over PIV techniques in high-speed facilities is that it is not limited by timing issues associated with tracer injection [12] or reduced particle response at Knudsen and Reynolds numbers [4] characteristic of high-speed wind tunnels. Methods of tagging velocimetry include the VENOM [13–17], APART [18–20], RELIEF [21–25], FLEET [26, 27], STARFLEET [28], PLEET [29], NO [30–34], argon [35], iodine [36, 37], sodium [38], acetone [39–41], NH [42] and the hydroxyl group techniques, [43–46] among others [47–52].

To recreate high-speed flow conditions for model and vehicle development, various facilities are used depending on the requirements [53]. In this work, the focus will be on impulse facilities, some of which are able to reproduce total flow enthalpy for short periods of time [54]. These facilities, which include shock and expansion tunnels, reproduce the flow velocity which can be important for research into mixing [55], thermo-chemical/fluid-mechanical interactions [56–58], and boundary-layer instability [59–61] and transition [62–64].

Challenges with making measurements in these facilities include vibration, short test times, experimental timing, harsh pre- and post-flow conditions, and in the case of particle-based techniques, particle injection [65]. Particle-based applications of velocimetry in impulse facilities include the impulsively started flow over a cylinder in a shock tube [66], PIV in shock tunnels [12], and shocked particle drag measurements [67]. Tagging velocimetry has also been applied in impulse facilities. Hydroxyl Tagging Velocimetry (HTV) was used to make measurements behind the bow shock wave that formed on a model in a shock tube [68]. Additionally, NO has been used as a tagging tracer to measure the freestream flow [34], and flow over test articles in reflected-shock tunnels [31].

In this paper, we focus on a version of tagging velocimetry called Krypton Tagging Velocimetry (KTV) as applied to flow over a sharp, hollow cylinder after the passage of the primary shock wave in the Stevens Shock Tube. Experiments are conducted in air and in N_2 that is doped with Kr. The experimental setup is described; namely, a simplified single-laser version of KTV that is justified by two-photon absorption cross-section calculations and emission spectra. Finally, results are presented from experiments conducted over a range of static thermodynamic conditions that are similar to larger-scale impulse hypersonic facilities to demonstrate KTV utility. These experimental results are compared to similarity solutions for compressible boundary-layer flow with excellent agreement.

II. SINGLE-LASER EXCITATION SCHEME FOR KTV

In this work, we focus on the use of Kr as a tracer for tagging velocimetry, which was first suggested by Mills *et al.* [69] and Balla and Everhart [70]. The key to the use of Kr as a tracer species for diagnostics is the two-photon transitions in the $\sim$ 190-220 nm range that are accessible with commercially available optics and laser systems. To date, KTV has been demonstrated by globally seeding high-speed N_2 flows with 1% Kr and air flows with 5% Kr. Applications include: 1) an underexpanded jet (first KTV demonstration) [71]; 2) mean and fluctuating turbulent boundary-layer profiles in a Mach 2.7 flow [72]; 3) 20+ simultaneous profiles of streamwise velocity and velocity fluctuations in a Mach 2.8 shock-wave/turbulent boundary-layer interaction [73]; and 4) the freestream of the large-scale AEDC Hypervelocity Tunnel 9 at Mach 10 and Mach 14 [74]. In these experiments, the researchers used a pulsed dye-laser to perform the write step at 214.7 nm to both form a write line and photosynthesize the metastable Kr tracer; after a prescribed delay, an additional pulsed dye-laser was used to re-excite the metastable Kr tracer to track displacement. Recently, simplified KTV schemes were developed and demonstrated in an underexpanded jet [75] where either: a) a pulsed-dye laser was used for the write step and a simple continuous-wave laser diode was used for the read step; or, b) successive images of the fluorescence from a single dye-laser pulse were used. In this work, a single-laser scheme is used to make the KTV measurements. In this work, we focus on the use of Kr as a tracer for tagging velocimetry, which was first suggested by Mills *et al.* [69] and Balla and Everhart [70]. The key to the use of Kr as a tracer species for diagnostics is the two-photon transitions in the $\sim$ 190-220 nm range that are accessible with commercially available optics and laser systems. To date, KTV has been demonstrated by globally seeding high-speed N_2 flows with 1% Kr and air flows with 5% Kr. Applications include: 1) an underexpanded jet (first KTV demonstration) [71]; 2) mean and fluctuating turbulent boundary-layer profiles in a Mach 2.7 flow [72]; 3) 20+ simultaneous profiles of streamwise velocity and velocity fluctuations in a Mach 2.8 shock-wave/turbulent boundary-layer interaction [73]; and 4) the freestream of the large-scale AEDC Hypervelocity Tunnel 9 at Mach 10 and Mach 14 [74]. In these experiments, the researchers used a pulsed dye-laser to perform the write step at 214.7 nm to both form a write line and photosynthesize the metastable Kr tracer; after a prescribed delay, an additional pulsed dye-laser was used to re-excite the metastable Kr tracer to track displacement. Recently, simplified KTV schemes were developed and demonstrated in an underexpanded jet [75] where either: a) a pulsed-dye laser was used for the write step and a simple continuous-wave laser diode was used for the read step; or, b) successive images of the fluorescence from a single dye-laser pulse were used. In this work, a single-laser scheme is used to make the KTV measurements.

Following the transitions marked in blue and red in the energy level diagram in Fig. 1 along with the relevant transition data in Table I (labeled as A, B, C etc.), the single-laser KTV scheme is performed as follows:
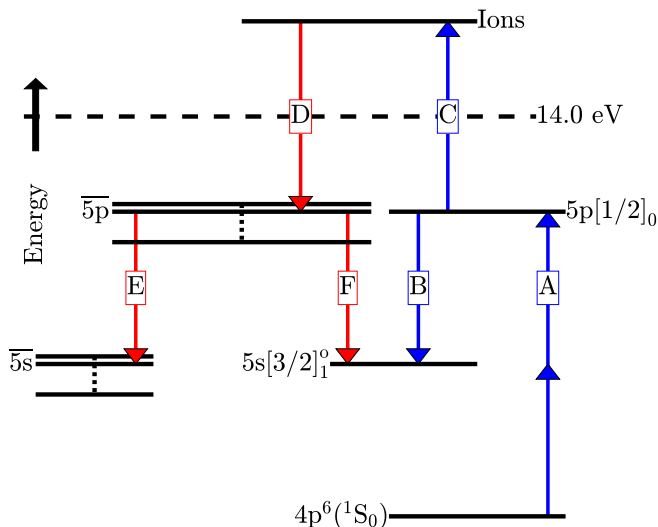
FIG. 1. Energy diagram with Racah $nl[K]_J$ notation for single-laser, (2+1) REMPI KTV scheme with excitation at 212.6 nm and successive camera gating (no read laser). Transition details in Table I. States $\overline{5p}$ and $\overline{5s}$ represent the numerous 5p and 5s states (tabulated in Table II) that are created by the recombination process. Transitions E and F represent the numerous transitions in the 5p-5s band. 14.0 eV marks ionization limit of Kr.

1. **Write Step:** Excite krypton atoms with a pulsed-tunable laser to form the tagged tracer through a (2+1) resonance-enhanced, multiphoton ionization (REMPI) process [76–80]. Firstly, two-photon excitation of $4p^6(^1S_0) \rightarrow 5p[1/2]_0$ (two 212.6 nm photons, transition A), and subsequent one-photon ionization (one 212.6 nm photon, transition C). Fluorescence for the write step is recorded primarily from the decay to the resonance state $5p[1/2]_0 \rightarrow 5s[3/2]_1^o$ (758.7 nm, transition B). Minor fluorescence contributions from transitions E and F, resulting from the recombination process (transition D) [81, 82] are also recorded. The position of the write line is marked by gated imaging of the laser-induced fluorescence (LIF) from these transitions, recorded with a camera positioned normal to the flow. The emission spectrum of this step is shown in black in Fig. 2.

2. **Read Step:** After a prescribed delay, record the displacement of the tagged krypton by gated imaging of the LIF from the residual $5p[1/2]_0 \rightarrow 5s[3/2]_1^o$ (758.7 nm) transition B, in addition to other transitions, E and F resulting from the recombination process, D. At this step, the fluorescence from transitions E and F dominate those of B. The emission spectrum of this step is shown in red or blue in Fig. 2.

Emission spectra were recorded to investigate the (2+1) REMPI process and extent of ionization of the fluorescing Kr atoms during the write/read steps. The

hypothesis was that if the spectra indicate transitions other than the $5p[1/2]_0 \rightarrow 5s[3/2]_1^o$ (758.7 nm) transition, the Kr atoms were at least partially ionized. As a result of the partially ionized Kr population, the fluorescence observed during the read step would be the result of the spontaneous emission from the byproducts of the Kr recombination process [81, 82]. This process occurs at a longer timescale than spontaneous emission in the absence of ionization, thus enabling the tagged Kr atoms to be imaged with sufficient signal-to-noise-ratio (SNR) during the read step without the need for a read laser.

The optical setup to record the spectra was identical to that used to record the data for the boundary-layer measurements (Fig. 5) with two exceptions. The experiments were conducted in quiescent flow, and, instead of imaging the fluorescing Kr atoms directly onto a camera, the Kr fluorescence was imaged onto the slit of an Oriel MS257, 25 cm spectrograph. The spectra were imaged with a Princeton Instruments PIMAX-4 (PM4-1024i-HR-FG-18-P46-CM) camera. The lens used was a Nikon NIKKOR 24-85mm f/2.8-4D with a 0.5 inch lens tube positioned at the spectrograph exit. This experimental setup was calibrated with a Kr pen lamp (Newport 6031).

The emission spectrum at three time increments after the write-laser pulse is presented in Fig. 2. We denote the time after the write-laser pulse as Δt, with the spectra recorded at $\Delta t = 0$ ns being representative of the write step, and the spectra recorded at $\Delta t = 500$ ns or $\Delta t = 1000$ ns being representative of the read step. The experiments were performed with a 212.6 nm wavelength, 3 mJ energy pulse in a 5 torr, 99% N_2/1% Kr mixture. The 758.7 nm transition dominated at $\Delta t = 0$ ns, corresponding to transition B in Fig. 1. From this, we conclude that the write-step fluorescence is dominated by the spontaneous emission from the $5p[1/2]_0 \rightarrow 5s[3/2]_1^o$ (758.7 nm) transition. For the spectra recorded at $\Delta t =$
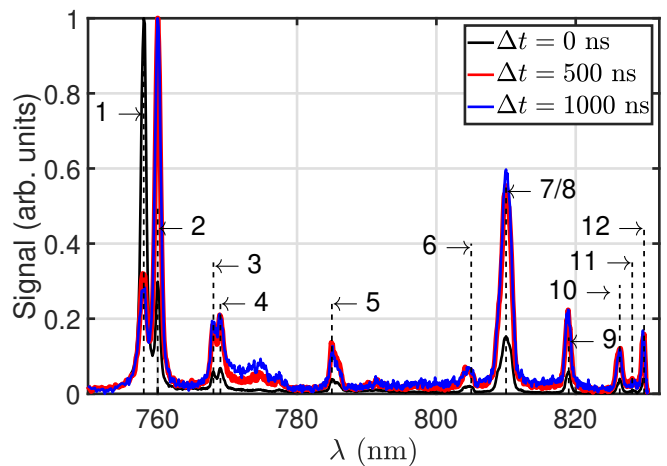

FIG. 2. Emission spectra for (2+1) REMPI process using $\lambda = 212.6$ nm excitation in a 99% N_2/1% Kr mixture. Atomic data for each line presented in Table II. Intensities normalized by maximum intensity at each time step.

500 ns and $\Delta t = 1000$ ns, many transitions are observed that are consistent with spontaneous emission from Kr atoms in the 5p states (Table II). From this, we conclude that the read-step fluorescence is due to the spontaneous emission from the byproducts of the Kr recombination process. We should note that we recorded spectra with 80 nm windows (e.g., 750-830 nm in Fig. 2) over a broad domain in the 400-850 nm range and recorded little or no signal outside of the 750-830 nm range. The emission results we present in Fig. 2 are consistent with those in the literature for ionized Kr; for example, see relative intensities (Table I) and energy-level diagram (Fig. 5) of Shiu and Biondi [81]. Additionally, we note that while maintaining laser intensity, detuning the laser wavelength off of the 212.6 nm resonance by a few picometers resulted in the complete loss of fluorescence. From this, we conclude that we are not photoionizing other constituents in the gas mixtures.

To understand the timescales of the tagged Kr lines, experiments were conducted where camera exposures of Kr fluorescence were recorded at successive times after the write-laser pulse, each with a 30 ns gate width. The optical setup for this series of experiments was identical to that in the boundary-layer measurements (Fig. 5), except the experiments were performed in a quiescent flow. Results are presented in Fig. 3 for both 99% N_2/1% Kr and 75% N_2/20% O_2/5% Kr mixtures. To estimate what the fluorescence signal behavior would be in the absence of ionization, we present a simple model. The population of the excited state $5p[1/2]_0$, N, is governed by $N = N_0 \exp(-Rt)$, where N_0 is the integration constant and $R = A_{ij} + Q$ is the sum of the Einstein coef-

ficient, A_{ij}, for transition B in Fig. 1 and the quenching rate, Q, which is estimated from Hsu $et\ al.$ [83]. The camera signal, F, at time t after the pulse, is then $F = \int_t^{t+\Delta t} N A_{ij} dt + n$, where Δt is the camera gate time and n is the noise level in the image [84]. Carrying out the integration gives,

$$F = (F_0 - n)\exp(-R(t - t_0)) + n, \qquad (1)$$

where F_0 is the initial signal at $t = t_0$. The initial condition, F_0, for Eq. (1) is prescribed as the signal count at the end of the laser pulse. The results in Fig. 3 show that the experiment and Eq. (1) are in reasonable agreement up to 20 ns after the laser pulse, after which, Eq. (1) predicts the signal to drop into the noise within 100 ns of the write-laser pulse. Note that in Fig. 3, the signal in air is higher in the beginning because of the extra krypton (5% vs 1% in N_2); however, the signal decays faster in air because of the quenching due to O_2, and after a certain point (~ 800 ns), the signal in air becomes lower than the signal in N_2.

The effects of pressure and mixture composition on the fluorescence signal are shown as Fig. 4. For a given gas mixture, the signal at the write step is higher for higher pressure cases because of increased Kr density. However, for the same high pressure cases, the signal at the read step may be lower because the quenching rate increases with pressure.

From the emission spectra (Fig. 2) and the time-resolved fluorescence results (Figs. 3 and 4), we conclude that the lifetime of the fluorescence signal is extended because the write-laser pulse is intense enough to partially ionize the Kr, and the recombination process is slow enough to enable a single-laser KTV technique.

The write-pulse energy requirement of the KTV scheme in this work is higher than that of previous schemes. Previous KTV schemes required two lasers, one for the write step and photosynthesis of the metastable state tracer, and one for the re-excitation from the metastable state on the read step. In this work, (2+1) REMPI and the recombination process are responsible for the long lifetime of the Kr fluorescence. For context on energy requirements, the previous two-laser scheme was able to write many lines with relatively low energy, as in Mustafa $et\ al.$ [73], where 20 lines with 350 µJ/line were used to investigate a Mach 3 shock-wave/turbulent boundary-layer interaction over a 20 mm x 20 mm domain. In this work, we have only a single line because of energy requirements, but the setup is simpler, and, as will be discussed later, has been demonstrated over a broad range of conditions in Kr-doped N_2 and air. We note that in Mustafa and Parziale [75], a scheme is presented where a simple, inexpensive diode laser was used for the read step in place of a complex dye-laser setup, and more work with the laser-diode strategy is forthcoming.
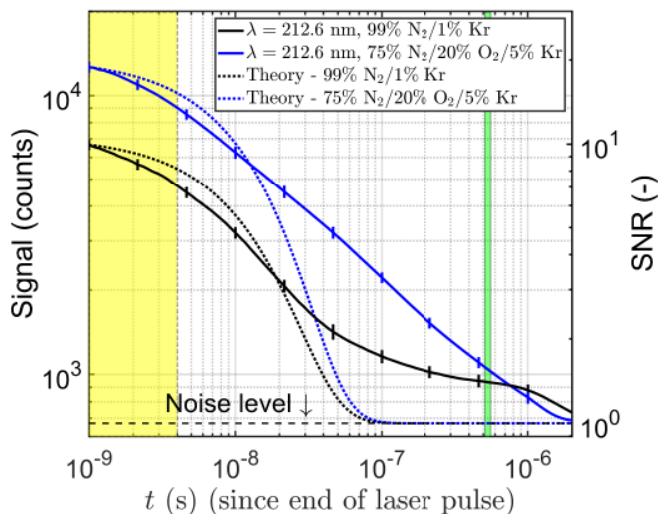

FIG. 3. Fluorescence curves for 99% N_2/1% Kr and 75% N_2/20% O_2/5% Kr at 5 torr for (2+1) REMPI process using $\lambda = 212.6$ nm excitation. Yellow and green regions are representative of the camera gate for write step and read step, respectively. Theory corresponds to Eq. (1). Vertical bars denote uncertainty.

TABLE I. **Relevant NIST Atomic Spectra Database Lines Data, labels match Fig. 1. Racah nl[K]$_J$ notation.**

Transition[a]	λ_{air} (nm)	Nature	A_{ki} (1/s)	E_i (cm^{-1})	E_k (cm^{-1})	Lower Level	Upper Level
A	212.56	Two-Photon	(-)	0	94092.8626	$4s^2 4p^6$, $^1S_0$	$5p[1/2]_2$
B	758.74	Single-Photon	4.3×10^7	80916.7680	94092.8626	$5s[3/2]_1^o$	$5p[1/2]_0$
C	212.56	Single-Photon	(-)	94092.8626	112914.433	$5p[1/2]_2$	Kr ions
E/F[b]	750-830	Single-Photon	10^6-10^7	80000	90000	$\overline{5s}$	$\overline{5p}$

[a] Transition D is not listed because it is not an atomic-level transition. It represents the recombination process.

[b] Entries in this row represent ranges and order of magnitude estimates since E and F in Fig. 1 represent numerous transitions in the 5p -5s band.
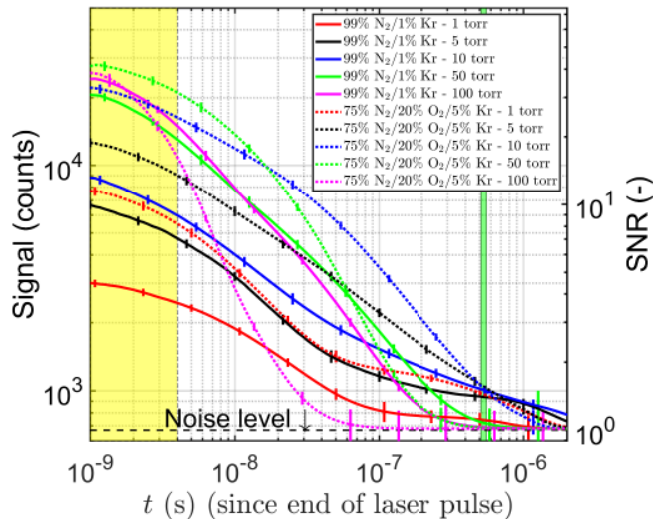

FIG. 4. Fluorescence curves for 99% N$_2$/1% Kr and 75% N$_2$/20% O$_2$/5% Kr at various pressures for (2+1) REMPI process using $\lambda = 212.6$ nm excitation. Yellow and green regions are representative of the camera gate for write step and read step, respectively. Vertical bars denote uncertainty.

TABLE II. **Atomic data for krypton spectra using $\lambda = 212.6$ nm two-photon excitation in N$_2$, Racah nl[K]$_J$ notation. Line numbers correspond to Fig. 2.**

Line	λ_{air} (nm)	Upper Level	Lower Level
1	758.74	$5p[1/2]_0$	$5s[3/2]_1^o$
2	760.15	$5p[3/2]_2$	$5s[3/2]_2^o$
3	768.52	$5p'[1/2]_0$	$5s'[1/2]_1^o$
4	769.45	$5p[3/2]_1$	$5s[3/2]_2^o$
5	785.48	$5p'[1/2]_1$	$5s'[1/2]_0^o$
6	805.95	$5p'[3/2]_1$	$5s'[1/2]_0^o$
7	810.44	$5p[5/2]_2$	$5s[3/2]_2^o$
8	811.29	$5p[5/2]_3$	$5s[3/2]_2^o$
9	819.01	$5p[3/2]_2$	$5s[3/2]_1^o$
10	826.32	$5p'[3/2]_2$	$5s'[1/2]_1^o$
11	828.11	$5p'[1/2]_1$	$5s'[1/2]_1^o$
12	829.81	$5p[3/2]_1$	$5s[3/2]_1^o$

III. CROSS-SECTION CALCULATIONS

In this section, we estimate Kr two-photon cross sections to justify the choice of excitation wavelength following the works of Lambropoulos [85] and Khambatta

et al. [86, 87]. To a first approximation, we assume that a larger two-photon cross-section will result in more effective (2+1) REMPI, and thus yield a larger fluorescence signal for the single-laser scheme used in this work.

The $5p[1/2]_0$ (212.6 nm) energy level (rather than the $5p[3/2]_2$ (214.7 nm) energy level) was used in this work because of its apparently larger two-photon cross-section. This observation appears to have first been made by Richardson *et al.* [88], where they observed an appreciable increase in the fluorescence signal when implementing Kr-PLIF, noting that they were likely not operating their laser in the ionization regime.

The two-photon excitation rate, W, is proportional to the cross section, $\sigma^{(2)}$, and the square of the photon flux, $\Phi = I/(h\nu_L)$, and can be written as

$$W = \sigma^{(2)}\Phi^2. \tag{2}$$

Clearly, an increase in cross section would increase the number of atoms in the higher energy state that can then be ionized with an additional photon. Plank's constant, the incident laser intensity, and the incident laser frequency are h, I, and ν_L, respectively. Following Lambropoulos [85], the two-photon cross section can be calculated as

$$\sigma^{(2)} = (2\pi)^3 \alpha^2 \omega_L^2 g(2\omega_L) \left|M_{fg}\right|^2, \tag{3}$$

where α is the fine structure constant and ω_L is the laser angular frequency. The line-shape function for two-photon excitation, $g(2\omega_L)$, is written on resonance as

$$g(2\omega_L = \omega_T) = \frac{2\sqrt{\ln(2)/\pi}}{\sqrt{2(\Delta\omega_L)^2 + (\Delta\omega_T)^2}}, \tag{4}$$

assuming the transition (Doppler broadened) and laser linewidths are Gaussians, and the full-width at half-maxima are $\Delta\omega_L$ and $\Delta\omega_T$ for the laser and transition, respectively.

The term M_{fg} represents the sum of the contributions to the two-photon cross section by individual channels with a ground state g, an intermediate state i, and a final state f. Following Lambropoulos [85], M_{fg} may be written as

$$M_{fg} = \sum_i \frac{<f|r^\lambda|i><i|r^\lambda|g>}{\omega_i - \omega_g - \omega_L}, \tag{5}$$

where the sum is over all possible intermediate states. Here, $< i|r^\lambda|g >$ represents the matrix element for the transition from the ground state to the intermediate state, and similarly, $< f|r^\lambda|i >$ represents the matrix element for the transition from the intermediate state to the final state. Following Khambatta *et al.* [86, 87], the matrix elements are calculated for linearly polarized light as

$$| < i|r^\lambda|g > |^2 =$$
$$(2J_i + 1) \begin{pmatrix} J_i & 1 & J_g \\ -M_i & 0 & M_g \end{pmatrix}^2 \frac{3hc_0^3\epsilon_0}{2e^2} \frac{A_{ig}}{\omega_{ig}^3}, \quad (6)$$

and

$$| < f|r^\lambda|i > |^2 =$$
$$(2J_f + 1) \begin{pmatrix} J_f & 1 & J_i \\ -M_f & 0 & M_i \end{pmatrix}^2 \frac{3hc_0^3\epsilon_0}{2e^2} \frac{A_{fi}}{\omega_{fi}^3}. \quad (7)$$

Here, J and M are the angular momentum and magnetic quantum numbers, respectively. The squared quantity in parentheses is the Wigner 3-j symbol. The physical constants h, c_0, ϵ_0, and e are Planck's constant, speed of light in a vacuum, permittivity of free space, and electron charge, respectively. Finally, A and ω are the Einstein coefficient and angular frequency of the transitions, respectively. This formulation gives the matrix elements in Eqs. 6 and 7 in units of m^2, assuming all physical constants are in meters-kilograms-seconds. We note that the results in Eqs. 6 and 7 are equivalent to those in Khambatta *et al.* [87] Section IV, Eq. (6), although their units are different.

In this work, the single-path approximation of Khambatta *et al.* [86] is used, where the summation over all intermediate states in Eq. (5) is reduced to a single term by considering only the resonance state, $5s[3/2]_1^0$, as the intermediate. Table III shows the two-photon cross sections for the $5p[1/2]_0$ and $5p[3/2]_2$ energy levels of krypton, corresponding to two-photon excitation using $\lambda = 212.6$ nm and $\lambda = 214.7$ nm, along with the corresponding atomic data used in the calculation. Furthermore, the magnetic quantum numbers are $M_g = M_i = M_f = 0$ for both energy levels because the laser is linearly polarized [89], and $\Delta\omega_L = 8.48 \times 10^9$ rad/s.

Our calculations indicate that the $5p[1/2]_0$ level has a larger two-photon cross-section than the $5p[3/2]_2$ level. This cross-section calculation, along with observations in our lab and others [88], justifies the use of the 212.6 nm excitation wavelength for the single-laser scheme in this work via efficient (2+1) REMPI.

IV. FACILITY AND EXPERIMENTAL SETUP

In this section, we give an overview of the experimental setup. The goal of these experiments is to demonstrate single-laser KTV in an impulse environment at static temperatures and pressures similar to those of a high-enthalpy impulse hypersonic facility. To this end, we will present measurements in the quasi-steady flow behind the primary shock wave in the Stevens Shock Tube over a hollow cylinder.

The laser setup in this work is considerably simpler than that of previous KTV techniques. The write-laser system is a frequency doubled Quanta Ray Pro-350 Nd:YAG laser and a frequency tripled Sirah PrecisionScan Dye Laser (DCM dye, DMSO solvent). The Nd:YAG laser pumps the dye laser with 1000 mJ/pulse at a wavelength of 532 nm. The dye laser is tuned to output a 637.7 nm beam, and frequency tripling (Sirah THU 205) of the dye-laser output results in a 212.6 nm beam, with 10 mJ energy, 1350 MHz linewidth, and 7 ns pulse width at a repetition rate of 10 Hz. The write beam was focused into the test section with a 200 mm focal-length, fused-silica lens. The beam fluence and spectral intensity at the waist were 43×10^3 J/cm^2 and 4.6×10^3 W/(cm^2 Hz), respectively. Additionally, we will present data with sufficient SNR 15 mm away from the focal point where the beam fluence and spectral intensity were 310 J/cm^2 and 33 W/(cm^2 Hz), respectively. We note here that the fluences and intensities are significantly higher than those in past KTV experiments with a two-laser setup.

The intensified CCD camera used for all experiments is a Princeton Instruments PIMAX-4 (PM4-1024i-HR-FG-18-P46-CM) with the Dual Image Feature (DIF) enabled. The lens used was a Nikon NIKKOR 24-85mm f/2.8-4D in "macro" mode that was positioned approximately 150 mm from the write/read location. The camera gate opens twice: first, for 5 ns immediately following the write-laser pulse; and, second, at a prescribed delay time of 500 ns for 50 ns to capture the residual fluorescence. The relative differences in gate width were chosen to address write/read ghosting issues while using the DIF with a short interframe delay. That is, the write image intensity was high and bleeding into the read image for longer values of write-image gate-width. The "phosphor decay time" of the P46 phosphor screen proved to be appropriate in this application. The specified ghosting value for a 500 ns interframe delay is 10%. The choice of 500 ns interframe delay was made to balance competing goals in tagging velocimetry: 1) A longer delay is sought to reduce the error in the measurement in the usual way per Eq. 17; 2) a shorter delay is sought to freeze as much of the fluid motion as possible (e.g, a 1 microsecond delay results in freezing structures on the order of 1 MHz or slower); and, 3) a shorter delay is sought for KTV because for higher pressure cases, the SNR is too low to make consistent measurements. Figs. 3 and 4 show that at about 1 microsecond, the SNR is too low for higher pressure cases.

A schematic of the measurement location in the Stevens Shock Tube is shown in Fig. 5. Optical access was provided by three fused-silica windows near the end of the tube. The operation of the shock tube is initiated by a diaphragm-piercing mechanism, consisting of a solenoid and a plunger. Three pressure transducers (see Fig. 6) are installed along the length of the tube, the

TABLE III. **Two-photon cross-sections and relevant atomic data.** W_{g1} and W_{1f} represent the Wigner 3-j symbols for the ground to intermediate and intermediate to final transitions receptively.

Level	λ	λ_{gi}	λ_{fi}	$\Delta\omega_T$	$g(2\omega_L=\omega_T)$	J_g	J_1	J_f	A_{ig}	A_{fi}	ω_{ig}	ω_{fi}	W_{ig}	W_{fi}	$\sigma^{(2)}$
(-)	(nm)	(nm)	(nm)	s^{-1}	s	(-)	(-)	(-)	(s^{-1})	(s^{-1})	(s^{-1})	(s^{-1})	(-)	(-)	(cm^4 s)
$5p[1/2]_0$	212.56	123.58	758.74	2.40×10^{10}	3.50×10^{-11}	0	1	0	2.98×10^8	4.31×10^7	1.52×10^{16}	2.48×10^{15}	$\left(-\sqrt{\tfrac{1}{3}}\right)$	$\left(-\sqrt{\tfrac{1}{3}}\right)$	6.00×10^{-46}
$5p[3/2]_2$	214.70	123.58	819.00	2.38×10^{10}	3.53×10^{-11}	0	1	2	2.98×10^8	8.94×10^6	1.52×10^{16}	2.29×10^{15}	$\left(-\sqrt{\tfrac{1}{3}}\right)$	$\left(+\sqrt{\tfrac{2}{15}}\right)$	3.16×10^{-46}

most downstream of which is at the measurement location (marked as "Pressure Transducer" in Fig. 5). There is also an additional port used to fill the driven section with gas mixtures. The experiments in this work were performed over a sectioned hollow cylinder with a sharp leading edge installed at the test location. The measurements were made in the $x-y_m$ coordinate system shown in Fig. 5 and were subsequently mapped to the $x-y$ coordinate system, as shown later. Fig. 6 shows sample pressure traces from experiments in N_2 in both x-t and P-t space, indicating a useful test time of ~ 1 ms.

The timing of the experiment is designed to keep the laser at operating temperature. As Fig. 7 shows, the laser and shock tube are controlled via pulse delay generators (PDG) and signal-conditioners/amplifiers (used for signal addition and inversion). The diaphragm rupture timing is set to a delay after the write-laser flashlamp pulse following experiment activation. The delay is chosen such that the laser and camera can be triggered upon arrival of the primary shock wave at the pressure transducer marked as "Pressure Transducer" in Fig. 5. This timing scheme kept the laser system on 8-12 Hz operation, which is close enough to specification for proper laser operation. In this setup, the laser timing dictates the shock tube timing, which was practical for developmental purposes in the lab. However, this timing strategy might not work in larger-scale shock tubes and tunnels, where there may be a 1-2 second delay between experiment initiation and the rupture of the primary diaphragm. With a conventional 10 Hz Nd:YAG/Dye-laser setup like the one used in this work, less laser power would be available if a delay on the order of 1 second was introduced into this timing scheme. However, advanced laser technology might serve to alleviate this concern, in addition to significantly increasing the repetition rate. Data in the literature suggests that the write step could be performed by ultra-fast lasers [88] or a tunable form of a burst-mode laser [90].

The boundary-layer measurements were made on a sectioned, sharp-leading-edge hollow-cylinder. In place of a flat plate, the cylindrical geometry was chosen because the write-laser beam could be propagated tangentially to the test article. This effectively increased the resolution near the wall by stretching the boundary layer and also reduced the effects of laser ablation on the test article surface.

The write laser excited Kr atoms on a line approximately tangent to the cylinder, and the camera captured the projected image of the line, y_m, and its displacement (sketch in Fig. 8). The locations of tagged Kr atoms on this cylinder were mapped to corresponding wall-normal points, y, over a flat plate to transform the curved-surface problem into a flat-plate problem for comparison to the similarity solution. The sketch in Fig. 8 is useful in the calculation of the mapped wall-normal location, y, as a function of the measurement distance y_m (the quantity measured from camera images). The radius of the cylinder is R, the angular offset from the true apogee, O, is
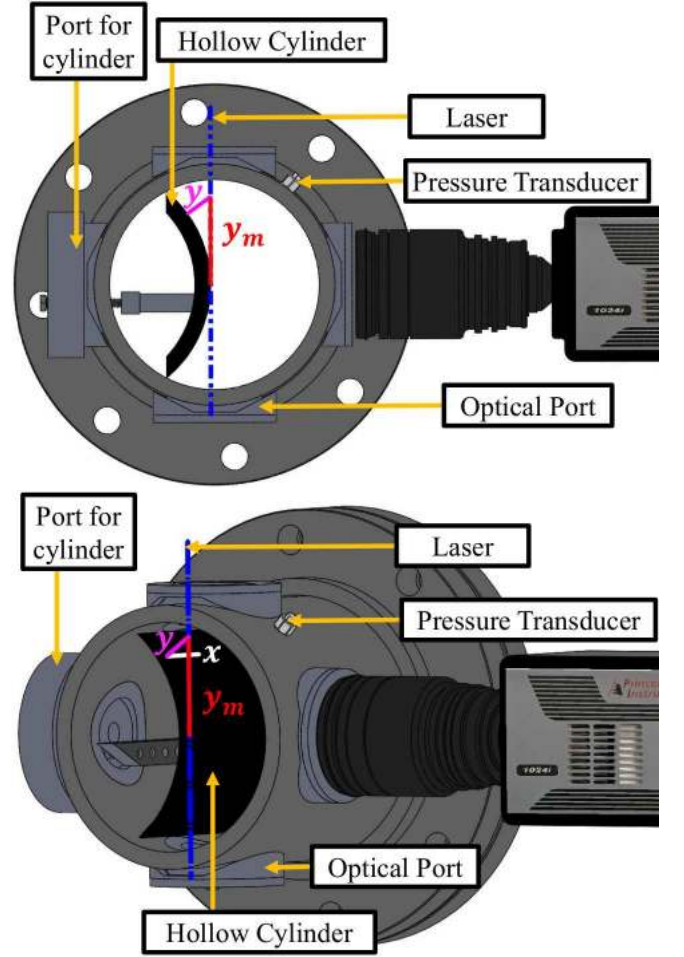

FIG. 5. Schematic of test article in shock tube. *Top:* Front view. Flow direction and x (streamwise) coordinate are into the paper, and along the surface of the cylinder. *Bottom:* Isometric view. y and y_m as in Fig. 8.

θ, and the wall location from the observed apogee, O^*, is y_w. The derivation of the mapping expression for y from y_m uses this geometry, beginning with the green and red triangles drawn in the sketch. From the green triangle, a relationship between θ and ϕ is obtained as

$$\sin(\theta + \phi) = \frac{R\sin(\theta) + y_w}{R}. \tag{8}$$

Solving Eq. (8) for ϕ gives,

$$\phi = \arcsin\left(\frac{R\sin(\theta) + y_w}{R}\right) - \theta. \tag{9}$$

To find the height of the red triangle, the distance y_d is found via,

$$y_d = \tan(\theta)y_m. \tag{10}$$

Applying the Pythagorean Theorem to the red triangle yields the final expression for the wall-normal distance,

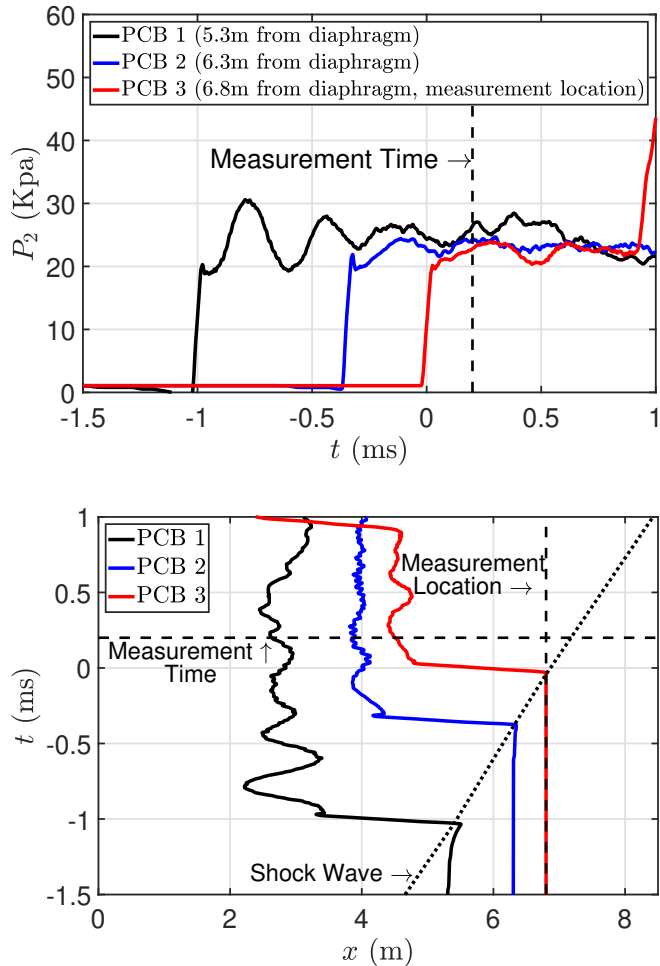$$y = \sqrt{(R\cos(\theta + \phi) - y_d)^2 + (R\sin(\theta) + y_m + y_w)^2} - R. \tag{11}$$
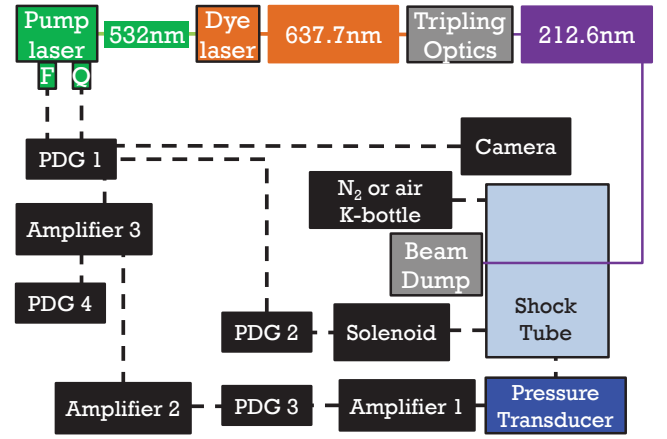

FIG. 7. Laser setup and timing for Stevens Shock Tube.

Fig. 9 shows the effects of y_w and θ on the mapping from y_m to y. The field of view of the current camera setup allows for a maximum y_m of approximately 20 mm. Importantly, it is observed that the effect of θ is small until about 20°, but the effects of y_w are significant. In these experiments $R = 84$ mm (size 6 pipe), $y_w \sim 0$-2 mm, and $\theta \sim 0°$.

FIG. 6. Representative pressure traces. Data corresponds to shot 169 in Table V. *Top: P-t* space. *Bottom: x-t* space.
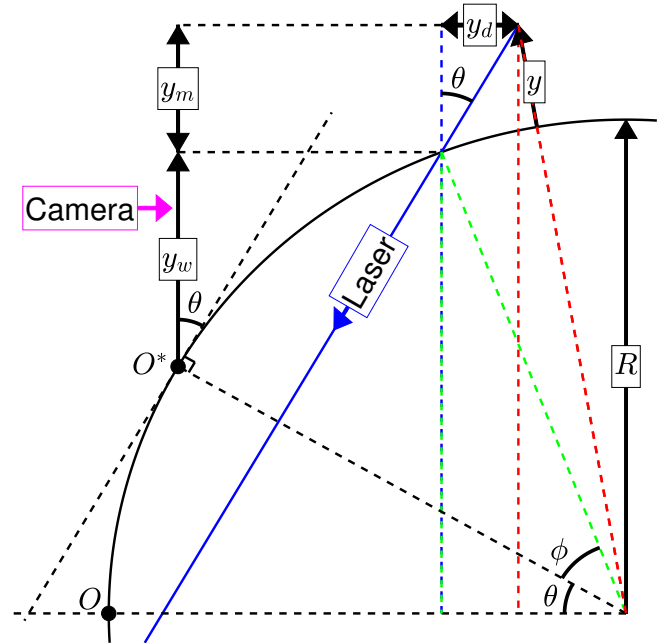

FIG. 8. Exaggerated sketch of the cylindrical surface (flow direction and streamwise coordinate, x, are out of the paper) and direction of laser propagation.
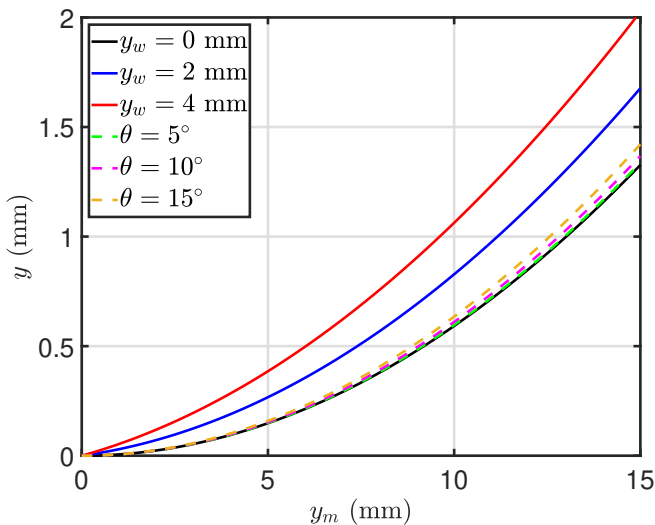
FIG. 9. Effect of θ and y_w on mapping to flat plate wall-normal location, y, as defined in Fig. 8.

TABLE IV. Experimental Conditions for 75% N_2/20% O_2/5% Kr driven gas mixture and helium as driver gas.

Shot	Re_2^{unit}	M_2	P_2	T_2	ρ_2	u_2	M_s	u_s
(-)	(m^{-1})	(-)	(kPa)	(K)	(kgm^{-3})	(ms^{-1})	(-)	(ms^{-1})
163	1.56×10^5	1.76	2.65	1410	0.007	1230	4.58	1520
162	3.80×10^5	1.74	6.30	1370	0.018	1200	4.47	1480
159	7.67×10^5	1.74	12.6	1370	0.035	1190	4.46	1480
157	1.15×10^6	1.74	19.0	1380	0.053	1200	4.48	1490

V. RUN CONDITIONS AND SIMILARITY SOLUTION FOR COMPRESSIBLE, LAMINAR BOUNDARY-LAYER FLOW

In these experiments, two gas mixtures were used in the driven section: 75% N_2/20% O_2/5% Kr to model air, and 99% N_2/1% Kr to model N_2. The driver gas in all cases was helium. The pressure ratio between the driver and driven sections was kept fixed at $P_4/P_1 = 380$, with both sections starting at room temperature, $T_4 = T_1 \sim 298$ K. This fixed the primary shock wave speed, which nominally fixed the post-shock-wave (state-2) temperature (T_2), velocity (u_2), and Mach number (M_2) with varying pressure (P_2) and density (ρ_2). This experimental design enabled a sweep of unit-Reynolds numbers from 1e5-1e6 m^{-1} with nominally fixed temperature and velocity. The run conditions are presented in Tables IV and V, calculated with Cantera [91] and the Shock and Detonation toolbox [92]. The inputs for these calculations were the initial pressure, P_1, in the driven section (state 1), the primary shock wave speed (as measured by pressure transducers), and the gas composition.

In addition, the similarity solution for a compressible boundary layer over a flat plate is used as a basis for

TABLE V. Experimental Conditions for 99% N_2/1% Kr driven gas mixture and helium as driver gas.

Shot	Re_2^{unit}	M_2	P_2	T_2	ρ_2	u_2	M_s	u_s
(-)	(m^{-1})	(-)	(kPa)	(K)	(kgm^{-3})	(ms^{-1})	(-)	(ms^{-1})
165	3.90×10^5	1.72	6.01	1300	0.016	1220	4.37	1510
166	7.71×10^5	1.73	12.3	1340	0.031	1250	4.42	1550
168	1.15×10^6	1.73	18.2	1330	0.047	1250	4.39	1540
169	1.54×10^6	1.73	24.5	1340	0.063	1240	4.41	1540

TABLE VI. Constants for Sutherland's viscosity law.

Gas	C_μ	S
(-)	(Pa s K$^{1/2}$)	(K)
Air	1.458×10^{-6}	110.4
N_2	1.407×10^{-6}	111

comparison to the KTV results mapped by Eq. (11). Following White [93], the equation governing momentum for a compressible, laminar boundary-layer flow over a flat plate is

$$(Cf'')' + ff'' = 0, \tag{12}$$

and the equation governing energy is

$$(Cg')' + Prfg' = -PrC(\gamma - 1)M_2^2 f''^2. \tag{13}$$

Here, $f' = u/u_2$, $g = \rho_2/\rho = T/T_2$, $C = \rho\mu/\rho_2\mu_2$ and the derivatives are with respect to the similarity variable $\eta = \left(\sqrt{u_2}\int_0^y \rho dy\right)/\sqrt{2\rho_2\mu_2 x}$. Following Kuehl [94], C is evaluated using Sutherland's Law as

$$C = \frac{C_\mu\sqrt{T_2}}{\mu_2}\frac{\sqrt{g}}{g + (S/T_2)} = C_0\frac{\sqrt{g}}{g + C_1}, \tag{14}$$

where C_μ and S are given in Table VI.

With this formulation, Eqs. 12 and 13 become,

$$f''' = \frac{g'f''}{g + C_1} - \frac{g'f''}{2g} - \frac{ff''(g + C_1)}{C_0\sqrt{g}}, \tag{15}$$

and

$$g'' = \frac{g'^2}{g + C_1} - \frac{g'^2}{2g} - Pr(\gamma - 1)M_2^2 f''^2 - \frac{Prfg'(g + C_1)}{C_0\sqrt{g}}. \tag{16}$$

The boundary conditions are $f(\eta = 0) = f'(\eta = 0) = 0$, $g(\eta = 0) = T_w/T_2$, and $f'(\eta \to \infty) = g(\eta \to \infty) = 1$. The KTV measurements were made at $x = 43\pm3$ mm from the leading edge. Fig. 10 shows representative temperature, density, and velocity profiles calculated using the similarity solution for the conditions in shot 169 in Table. V.
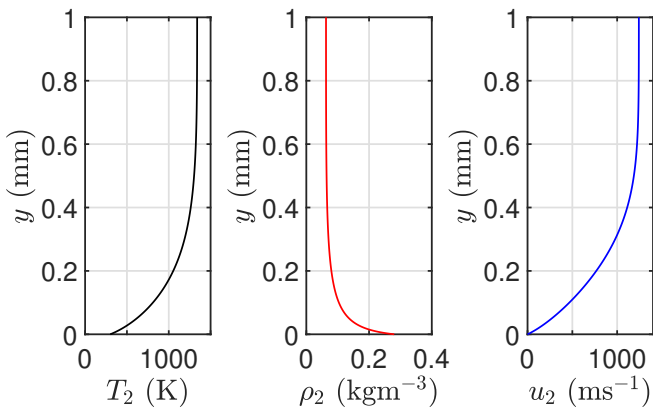
FIG. 10. Representative temperature, density, and velocity profiles calculated from similarity solution. Conditions correspond to shot 169 in Table V.

VI. DATA REDUCTION AND UNCERTAINTY ESTIMATE

In this section, we discuss how the data are reduced and we estimate the uncertainty of the KTV measurements. To process the KTV exposures, the line centers were found in the following way:

1) Crop the image to an appropriate field of view.
2) Apply a two-dimensional Wiener adaptive-noise removal filter.
3) Convert the images to double precision numbers and normalize the intensity to fall in the range of 0-1.
4) Apply the Gaussian peak finding algorithm from O'Haver [95] to find the line center for the top row using the read line in the top row of each image as an initial guess.
5) Proceeding from the top-down, apply the Gaussian peak finding algorithm from O'Haver [95] to find the line center for each row using the line center location immediately above as the initial guess.

No binning of the data was performed, and a vertical and horizontal calibration length-scale (51.32 pixels/mm) was taken in the $x - y_m$ plane prior to the experiments.

Error bars for the KTV measurements are calculated in the same fashion as in Zahradka et $al.$ [72] as

$$\widetilde{U} = \sqrt{\left(\widetilde{\Delta x}\frac{\partial U}{\partial \Delta x}\right)^2 + \left(\widetilde{\Delta t}\frac{\partial U}{\partial \Delta t}\right)^2 + \left(v'_{RMS}\frac{\partial U}{\partial y}\Delta t\right)^2}, \quad (17)$$

where uncertainty estimates of a variable are indicated with a tilde. The uncertainty in the measured displacement distance, $\widetilde{\Delta x}$, of the tracer is estimated as 10 μm, from the 95% confidence bound on the write and read locations from the Gaussian fits. The uncertainty in time, $\widetilde{\Delta t}$, is estimated to be the camera gate width, 50 ns, which causes fluorescence blurring as considered in Bathel et $al.$ [33]. The third term in Eq. (17) is uncertainty in streamwise velocity due to wall-normal flow in

the xy-plane. This formulation is taken from Hill and Klewicki [96] and Bathel et $al.$ [33]. The wall-normal fluctuations used in Eq. (17) (v'_{RMS}) are conservatively estimated to be 10% of the edge velocity.

VII.   RESULTS AND DISCUSSION

In this section, single-shot KTV measurements and similarity-solution calculations are presented and discussed for the Kr-doped air and N_2 experiments. In Figs. 11 and 12, we present results for each case at four unit Reynolds numbers, increasing top to bottom, with three plots in one box for each experiment. Corresponding flow conditions are listed in Tables IV and V. For each experiment, the plots on the left are the superposed, unmapped "write" and "read" KTV images, both of which were intensity normalized prior to superposition. The field-of-view of KTV measurements in these figures is ~ 20 mm. The plots in the center for each case are the superposed, mapped (cylinder to a flat plate) "write" and "read" KTV images, both of which were intensity normalized prior to superposition. For each case, the plots on the right show the similarity solution in blue, and the KTV velocity profile in black with error bars in red as derived from Eq. (17).

The agreement between the KTV derived velocity profiles and the similarity solutions is excellent in Figs. 11 and 12. Because of our experimental design, the edge Mach number is constant, so we observe that the boundary-layer thickness is reduced with increasing Reynolds number; this follows the typical scaling of compressible-boundary-layer thickness as $\delta \propto M^2/\sqrt{Re}$ [93]. The KTV derived velocity profiles are collapsed by normalizing the profile by the edge velocity and plotting against the similarity variable in Fig. 13. The similarity variable is $\eta = \left(\sqrt{u_2}\int_0^y \rho(y)dy\right)/\sqrt{2\rho_2\mu_2 x}$, where the density profile, $\rho(y)$, is calculated from the similarity solution. In Fig. 13, there is a weak inflection point at $\eta \sim 1$, and for the larger boundary-layer thickness cases, the KTV data is able to bear this inflection point out; however, improvements to the SNR would have to be made to do this reliably at all conditions.

In Figs. 11 and 12, we were able to resolve the velocity very close to the wall, down to $y \sim 50$ μm. The signal-to-noise ratio (SNR) is appropriate for velocity profile extraction in all cases. We note that within the boundary layer, the SNR decreases because of the deformation of the tagged line due to the shear stress. This decrease in signal makes boundary-layer measurements notably more difficult than freestream measurements, which is consistent with past experience [73]. This means that boundary-layer measurements require higher laser power than freestream measurements. Furthermore, the "write" and "read" line thicknesses are nominally equal (~ 300 μm), which is consistent with past KTV experiments in Fig. 6 of Zahradka et $al.$ [72]. This indicates that there is minimal thermal expansion due to rapid gas
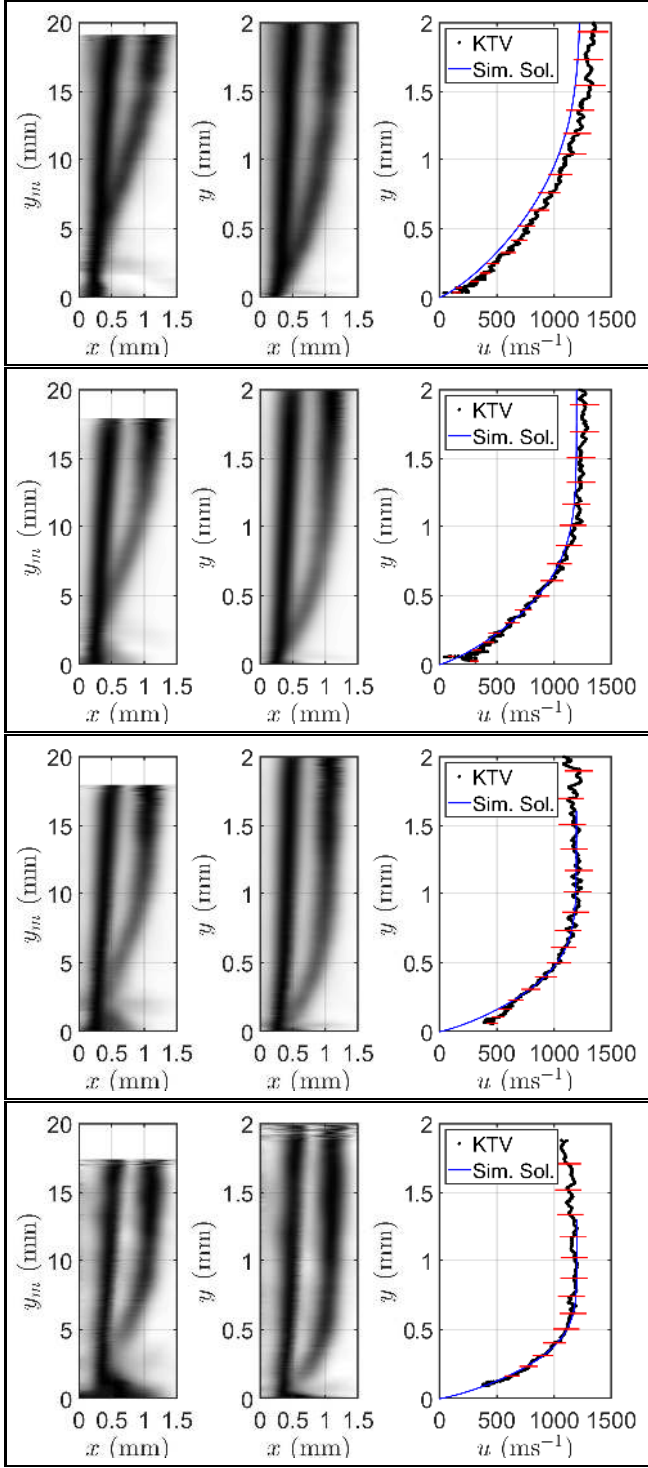
FIG. 11. Results for KTV experiments in 75% N_2/20% O_2/5% Kr. From top: $Re_2^{unit} = 1.55\times10^5$ m^{-1} (shot 163), $Re_2^{unit} = 3.80\times10^5$ m^{-1} (shot 162), $Re_2^{unit} = 7.63\times10^5$ m^{-1} (shot 159), $Re_2^{unit} = 1.15\times10^6$ m^{-1} (shot 157). *Left:* Superposition of raw write and read KTV images (inverted Scale). *Center:* Superposition of write and read images mapped from y_m to y (black). *Right:* Similarity solution in blue and KTV derived velocity profile in black with error bars in red.
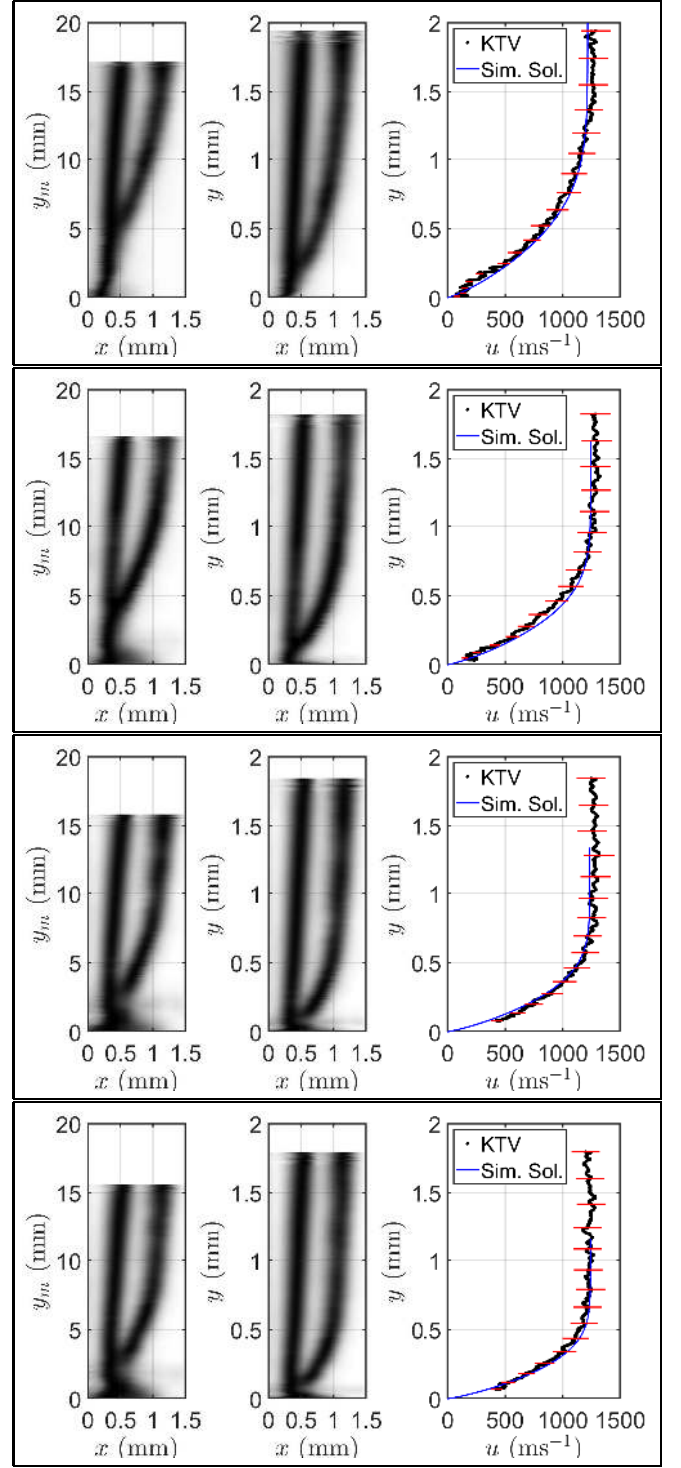
FIG. 12. Results for KTV experiments in 99% N_2/1%. From top: $Re_2^{unit} = 3.88\times10^5$ m^{-1} (shot 165), $Re_2^{unit} = 7.68\times10^5$ m^{-1} (shot 166), $Re_2^{unit} = 1.15\times10^6$ m^{-1} (shot 168), $Re_2^{unit} = 1.53\times10^6$ m^{-1} (shot 159). *Left:* Superposition of raw write and read KTV images (inverted Scale). *Center:* Superposition of write and read images mapped from y_m to y (black). *Right:* Similarity solution in blue and KTV derived velocity profile in black with error bars in red.

heating from the write-laser pulse. That is, this experimental method imparts minimal perturbations to the sensitive laminar boundary-layer during measurement.

The signal count at the read step as a function of static pressure, P_2, for the air and N_2 mixtures is presented in Fig. 14. Initially, with increasing pressure, SNR in both mixtures increases due to the increased krypton density. However, with increasing pressure, there is a tradeoff between the increase in SNR due to higher krypton density and the decrease in SNR associated with the quenching of the excited tagged line. The increase in krypton density is initially the dominant effect up to a critical point, 12 kPa for N_2 and 6 kPa for air in these experiments. After this, the SNR starts to decrease with increasing pressure, indicating that the quenching effect is overtaking the effect of larger krypton density. Additionally, we can see that in Fig. 14, measurements could have been made at higher static pressure, P_2, for the N_2 experiments, but the Stevens Shock Tube could not produce these conditions.

FIG. 14. Read step signal count vs. static pressure, P_2, in air and N_2 mixtures at the boundary layer edge.
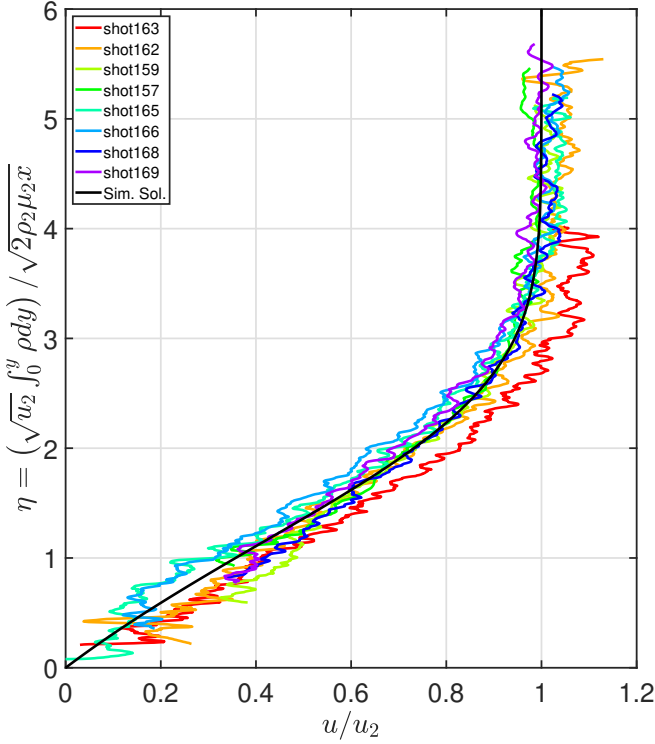

FIG. 13. Collapse of KTV derived velocity profiles and comparison to the similarity solution for compressible boundary-layer flow.

VIII. UTILITY OF OFF-SURFACE MEASUREMENTS

In this section, we present an example where off-surface measurements capture flow features that would otherwise be difficult to glean by surface measurements of pressure,
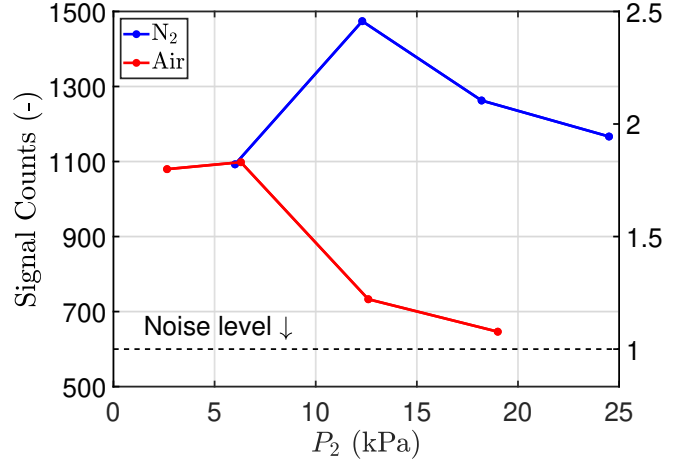
temperature, or heat transfer. Fig. 15 shows the results of an experiment in the Stevens Shock Tube performed with an air driver and a driven section of 99% N_2/1% Kr where the post-shock conditions were $P_2 = 4.7$ kPa, $T_2 = 635$ K, $u_2 = 613$ ms^{-1} and $M_2 = 1.2$. The KTV derived velocity profile clearly shows that the flow is not established over the hollow cylinder. The most likely reason was that the post-shock Mach number, M_2, was not high enough to have an attached shock wave on the sharp-angled cut at the leading edge of the inner surface of the hollow cylinder. This non-established flow was part of the reason why we chose to use a helium driver for the experiments presented in Section VII. Using a helium driver increased M_2 such that the shock wave over the sharp-angled cut on the inner surface was attached; as such, the flow over the hollow cylinder was quickly established, and we were able to seek comparison to the similarity solutions. Surface measurements may have had more difficulty identifying this behavior. Consequently,
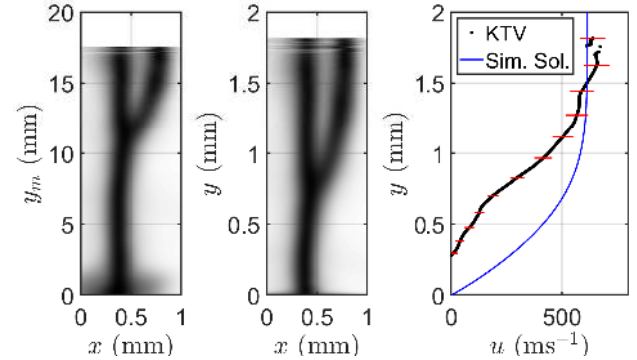

FIG. 15. Example of non-established flow in 99% N_2/1% Kr. *Left:* Superposition of raw write and read KTV images. *Center:* Superposition of write and read images mapped from y_m to y. *Right:* Similarity solution in blue and KTV derived velocity profile in black with error bars in red.

to determine whether the flow has been established in an experiment, especially in impulse facilities, off-surface measurements are invaluable.

IX. CONCLUSIONS

A single-laser Krypton Tagging Velocimetry (KTV) setup was used to study the quasi-steady flow behind the primary shock wave over a hollow cylinder in the Stevens Shock Tube. The (2+1) resonance-enhanced, multiphoton ionization (REMPI) of Kr with an excitation wavelength of $\lambda = 212.6$ nm was used to create the tracer whose fluorescence was imaged at successive times.

Relative to previous two-laser KTV schemes, this single-laser approach has the advantage of being simpler and more cost-effective but has a higher laser energy requirement. Emission spectra and the time-resolved fluorescence data were presented to support the assertion that the lifetime of the fluorescence signal is extended beyond the spontaneous emission timescale because the write-laser pulse is intense enough to partially ionize the Kr. The resulting recombination process occurs on a relatively slow timescale (~ 1 μs), thus enabling a single-laser KTV technique. The choice of excitation wavelength was justified by two-photon absorption cross-section calculations.

KTV derived velocity profiles were recorded over a sectioned, sharp-edged hollow cylinder by propagating the write-laser beam tangentially to the cylinder surface. These results were then mapped to wall-normal locations corresponding to a flat plate for comparison to similarity solutions for a compressible, laminar boundary layer. Agreement between the similarity solutions and the KTV derived data was excellent in all cases.

Eight experiments were performed in two gas mixtures: a) 99% N_2/1% Kr at post-shock temperature T_2=1300 K, pressure range $P_2 = 6.0 - 25$ kPa, and unit Reynolds number range $Re_2 = 3.9 \times 10^5 - 1.54 \times 10^6$ m^{-1}; and, b) in 75% N_2/20% O_2/5% Kr at post-shock temperature $T_2 =1400$ K, pressure range $P_2 = 2.7 - 19$ kPa, and unit Reynolds number range $Re_2 = 1.56 \times 10^5 - 1.15 \times 10^6$ m^{-1}. Notably, the range of static conditions spans those typical of large-scale, high-enthalpy hypersonic impulse facilities, albeit at lower total enthalpy; that is, the freestream pressure and temperature (but not the velocity) of large-scale facilities were reproduced to demonstrate KTV utility.

Additionally, we presented an example where the KTV derived velocity profile clearly shows that the flow is not established over the hollow cylinder. We came to the conclusion that the post-shock Mach number, M_2, was not high enough to have an attached shock wave on the sharp-angled cut at the leading edge of the inner surface of the hollow cylinder. This is a demonstration that off-surface measurements, like KTV, capture flow features that would otherwise be difficult to obtain by surface measurements alone, especially in impulse facilities.

Challenges and limitations associated with this measurement technique included experiment timing, laser-energy requirements, and surface ablation. As is the case in impulse facilities, the short test time (~ 1 ms) required the use of a complex timing circuit that delayed and subsequently triggered the laser pulse upon arrival of the primary shock wave. The comparatively large laser energy requirement is crucial to this technique, as it relies on using ionized Kr as the tracer particles. This requirement precluded tagging multiple lines in the flow, as splitting the laser beam would have resulted in insufficient energy per line. Furthermore, the use of this technique in air at pressures higher than 19 kPa requires more than the 10 mJ/pulse currently possible with this laser system. The ablation of the model presents a challenge in that the resulting plume near the surface obscures the desired tagged line. Therefore, measurements where the laser-beam-model-grazing strategy is not employed would be more difficult.

The next step is to implement KTV in a large-scale, high-enthalpy impulse hypersonic facility. We should note that because of the way that error is handled in tagging velocimetry (Eq. (17)), the uncertainty would be reduced in high-enthalpy impulse facilities where the velocity is significantly higher. There are experimental timing issues with a conventional 10 Hz Nd:YAG/Dye-laser setup like the one used in this work. However, advanced laser technology might serve to alleviate this concern, in addition to significantly increasing the repetition rate. Data in the literature suggests that the write step could be performed by ultra-fast lasers [88] or a tunable form of a burst-mode laser [90]. Furthermore, the use of such lasers will enable us to reach converged statistics when studying unsteady flows in impulse facilities. For example, given a laser with a 10 kHz repetition rate, we would be able to acquire 500 samples in ~ 100 ms, which is the typical test time of Ludweig tubes. With a 100 kHz repetition rate, the required test time would be ~ 10 ms, which is typical of shock tunnels.

X. ACKNOWLEDGMENTS

[1] P. M. Danehy, J. Weisberger, C. Johansen, D. Reese, T. Fahringer, N. J. Parziale, C. Dedic, J. Estevadeordal, and B. A. Cruden, "Non-Intrusive Measurement Techniques for Flow Characterization of Hypersonic Wind Tunnels," in *Flow Characterization and Modeling of Hypersonic Wind Tunnels (NATO Science and Technology Organization STO-AVT 325)* (Von Karman Institute, Brussels, Belgium, 2018).

[2] S. J. Beresh, J. F. Henfling, R. W. Spillers, and S. M. Spitzer, "Postage-stamp PIV: Small Velocity Fields at 400 kHz for Turbulence Spectra Measurements," Measurement Science and Technology **29** (2017).

[3] F. Scarano, "Overview of PIV in Supersonic Flows," in *"Particle Image Velocimetry: New Developments and Recent Applications"* ("Springer Berlin Heidelberg", "Berlin, Heidelberg", "2008") pp. "445–463".

[4] E.. Loth, "Compressibility and Rarefaction Effects on Drag of a Spherical Particle," AIAA Journal **46**, 2219–2228 (2008).

[5] D. Ragni, F. Schrijer, B. W. van Oudheusden, and F. Scarano, "Particle tracer response across shocks measured by PIV," Experiments in Fluids **50**, 53–64 (2011).

[6] G. E. Elsinga and G. C. Orlicz, "Particle imaging through planar shock waves and associated velocimetry errors," Experiments in Fluids **56**, 129 (2015).

[7] D. Mitchell, D. Honnery, and J. Soria, "Particle relaxation and its influence on the particle image velocimetry cross-correlation function," Experiments in Fluids **51**, 933 (2011).

[8] O. J. H. Williams, T. Nguyen, A.-M. Schreyer, and A. J. Smits, "Particle response analysis for particle image velocimetry in supersonic flows," Physics of Fluids **27**, 076101 (2015).

[9] K. T. Lowe, Gwibo. Byun, and R. L. Simpson, "The Effect of Particle Lag on Supersonic Turbulent Boundary Layer Statistics," in *Proceedings of AIAA SciTech 2014* (AIAA-2014-0233, National Harbor, Maryland, 2014).

[10] J. M. Brooks, A. K. Gupta, M. S. Smith, and E. C. Marineau, "Particle image velocimetry measurements of Mach 3 turbulent boundary layers at low Reynolds numbers," Experiments in Fluids **59**, 83 (2018).

[11] M. M. Koochesfahani and D. G. Nocera, "Molecular Tagging Velocimetry," in *Springer Handbook of Experimental Fluid Mechanics*, edited by C. Tropea, A. L. Yarin, and J. F. Foss (Springer, 2007).

[12] J. Haertig, M. Havermann, C. Rey, and A. George, "Particle Image Velocimetry in Mach 3.5 and 4.5 Shock-Tunnel Flows," AIAA Journal **40**, 1056–1060 (2002).

[13] A. G. Hsu, R. Srinivasan, R. D. W. Bowersox, and S. W. North, "Molecular Tagging Using Vibrationally Excited Nitric Oxide in an Underexpanded Jet Flowfield," AIAA Journal **47**, 2597–2604 (2009).

[14] A. G. Hsu, R. Srinivasan, R. D. W. Bowersox, and S. W. North, "Two-component molecular tagging velocimetry utilizing NO fluorescence lifetime and NO_2 photodissociation techniques in an underexpanded jet flowfield," Applied Optics **48**, 4414–4423 (2009).

[15] R. Sánchez-González, R. Srinivasan, R. D. W. Bowersox, and S. W. North, "Simultaneous velocity and temperature measurements in gaseous flow fields using the venom technique," Optics Letters **36**, 196–198 (2011).

[16] R. Sánchez-González, R. D. W. Bowersox, and S. W. North, "Simultaneous velocity and temperature measurements in gaseous flowfields using the vibrationally excited nitric oxide monitoring technique: a comprehensive study," Applied Optics **51**, 1216–1228 (2012).

[17] R. Sánchez-González, R. D. W. Bowersox, and S. W. North, "Vibrationally excited NO tagging by $NO(A^2\Sigma^+)$ fluorescence and quenching for simultaneous velocimetry and thermometry in gaseous flows," Optics Letters **39**, 2771–2774 (2014).

[18] N. Dam, R. J. H. Klein-Douwel, N. M. Sijtsema, and J. J. ter Meulen, "Nitric oxide flow tagging in unseeded air," Optics Letters **26**, 36–38 (2001).

[19] N. M. Sijtsema, N. J. Dam, R. J. H. Klein-Douwel, and J. J. ter Meulen, "Air Photolysis and Recombination Tracking: A New Molecular Tagging Velocimetry Scheme," AIAA Journal **40**, 1061–1064 (2002).

[20] W. P. N. Van der Laan, R. A. L. Tolboom, N. J. Dam, and J. J. ter Meulen, "Molecular tagging velocimetry in the wake of an object in supersonic flow," Experiments in Fluids **34**, 531–534 (2003).

[21] R. Miles, C. Cohen, J. Connors, P. Howard, S. Huang, E. Markovitz, and G. Russell, "Velocity measurements by vibrational tagging and fluorescent probing of oxygen," Optics Letters **12**, 861–863 (1987).

[22] R.B. Miles, J.J. Connors, E.C. Markovitz, P.J. Howard, and G.J. Roth, "Instantaneous profiles and turbulence statistics of supersonic free shear layers by Raman excitation plus laser-induced electronic fluorescence (RELIEF) velocity tagging of oxygen," Experiments in Fluids **8**, 17–24 (1989).

[23] R. B. Miles, D. Zhou, B. Zhang, and W. R. Lempert, "Fundamental Turbulence Measurements by RELIEF Flow Tagging," AIAA Journal **31**, 447–452 (1993).

[24] R. B. Miles and W. R. Lempert, "Quantitative Flow Visualization in Unseeded Flows," Annual Review of Fluid Mechanics **29**, 285–326 (1997).

[25] R. B. Miles, J. Grinstead, R. H. Kohl, and G. Diskin, "The RELIEF flow tagging technique and its application in engine testing facilities and for helium-air mixing studies," Measurement Science and Technology **11**, 1272–1281 (2000).

[26] J. B. Michael, M. R. Edwards, A. Dogariu, and R. B. Miles, "Femtosecond laser electronic excitation tagging for quantitative velocity imaging in air," Applied Optics **50**, 5158–5162 (2011).

[27] M. R. Edwards, A. Dogariu, and R. B. Miles, "Simultaneous Temperature and Velocity Measurements in Air with Femtosecond Laser Tagging," AIAA Journal **53**, 2280–2288 (2015).

[28] N. Jiang, B. R. Halls, H. U. Stauffer, P. M. Danehy, J. R. Gord, and S. Roy, "Selective two-photon absorptive resonance femtosecond-laser electronic-excitation tagging velocimetry," Optics Letters **41**, 2225–2228 (2016).

[29] N. Jiang, J. G. Mance, M. N. Slipchenko, J. J. Felver, H. U. Stauffer, T. Yi, P. M. Danehy, and S. Roy, "Seedless velocimetry at 100 khz with picosecond-laser electronic-excitation tagging," Optics Letters **42**, 239–242 (2017).

[30] P. M. Danehy, P. Mere, M. J. Gaston, S. O'Byrne, P. C. Palma, and A. F. P. Houwing, "Fluorescence Velocime-

try of the Hypersonic, Separated Flow over a Cone," AIAA Journal **39**, 1320–1328 (2001).

[31] P. M. Danehy, S. O'Byrne, A. F. P. Houwing, J. S. Fox, and D. R. Smith, "Flow-tagging Velocimetry for Hypersonic Flows using Fluorescence of Nitric Oxide," AIAA Journal **41**, 263–271 (2003).

[32] J. Bominaar, M. Pashtrapanska, T. Elenbaas, N. Dam, H. Ter Meulen, and W. van de Water, "Writing in turbulent air," Physical Review E **77**, 046312 (2008).

[33] B. F. Bathel, P. M. Danehy, J. A. Inman, S. B. Jones, C. B. Ivey, and C. P. Goyne, "Velocity Profile Measurements in Hypersonic Flows Using Sequentially Imaged Fluorescence-Based Molecular Tagging," AIAA Journal **49**, 1883–1896 (2011).

[34] P. Matos, L. G. Barreta, and C. A. Martins, "Velocity and NO-Lifetime Measurements in an Unseeded Hypersonic Air Flow," Journal of Fluids Engineering **140**, 121105 (2018).

[35] J. L. Mills, *Investigation of Multi-Photon Excitation in Argon with Applications in Hypersonic Flow Diagnostics*, Ph.D. thesis, Old Dominion University (2016).

[36] J. C. McDaniel, B. Hiller, and R. K. Hanson, "Simultaneous multiple-point velocity measurements using laser-induced iodine fluorescence," Optics Letters **8**, 51–53 (1983).

[37] R. J. Balla, "Iodine Tagging Velocimetry in a Mach 10 Wake," AIAA Journal **51**, 1–3 (2013).

[38] P. Barker, A. Bishop, and H. Rubinsztein-Dunlop, "Supersonic velocimetry in a shock tube using laser enhanced ionisation and planar laser induced fluorescence," Applied Physics B **64**, 369–376 (1997).

[39] W. R. Lempert, N. Jiang, S. Sethuram, and M. Samimy, "Molecular Tagging Velocimetry Measurements in Supersonic Microjets," AIAA Journal **40**, 1065–1070 (2002).

[40] W. R. Lempert, M. Boehm, N. Jiang, S. Gimelshein, and D. Levin, "Comparison of molecular tagging velocimetry data and direct simulation monte carlo simulations in supersonic micro jet flows," Experiments in Fluids **34**, 403–411 (2003).

[41] T. Handa, K. Mii, T. Sakurai, K. Imamura, S. Mizuta, and Y. Ando, "Study on supersonic rectangular microjets using molecular tagging velocimetry," Experiments in Fluids **55**, 1–9 (2014).

[42] S. Zhang, X. Yu, H. Yan, H. Huang, and H. Liu, "Molecular tagging velocimetry of NH fluorescence in a high-enthalpy rarefied gas flow," Applied Physics B **123**, 122 (2017).

[43] L. R. Boedeker, "Velocity measurement by H_2O photolysis and laser-induced fluorescence of OH," Optics Letters **14**, 473–475 (1989).

[44] J. A. Wehrmeyer, L. A. Ribarov, D. A. Oguss, and R. W. Pitz, "Flame Flow Tagging Velocimetry with 193-nm H_2O Photodissociation," Applied Optics **38**, 6912–6917 (1999).

[45] R. W. Pitz, M. D. Lahr, Z. W. Douglas, J. A. Wehrmeyer, S. Hu, C. D. Carter, K.-Y. Hsu, C. Lum, and M. M. Koochesfahani, "Hydroxyl tagging velocimetry in a supersonic flow over a cavity," Applied Optics **44**, 6692–6700 (2005).

[46] M. A. André, P. M. Bardet, R. A. Burns, and P. M. Danehy, "Characterization of hydroxyl tagging velocimetry for low-speed flows," Measurement Science and Technology **28**, 085202 (2017).

[47] B. Hiller, R. A. Booman, C. Hassa, and R. K. Hanson, "Velocity visualization in gas flows using laser-induced phosphorescence of biacetyl," Review of Scientific Instruments **55**, 1964–1967 (1984).

[48] C. P. Gendrich and M. M. Koochesfahani, "A spatial correlation technique for estimating velocity fields using molecular tagging velocimetry (MTV)," Experiments in Fluids **22**, 67–77 (1996).

[49] C. P. Gendrich, M. M. Koochesfahani, and D. G. Nocera, "Molecular tagging velocimetry and other novel applications of a new phosphorescent supramolecule," Experiments in Fluids **23**, 361–372 (1997).

[50] B. Stier and M. M. Koochesfahani, "Molecular tagging velocimetry (MTV) measurements in gas phase flows," Experiments in Fluids **26**, 297–304 (1999).

[51] L. A. Ribarov, J. A. Wehrmeyer, F. Batliwala, R. W. Pitz, and P. A. DeBarber, "Ozone Tagging Velocimetry Using Narrowband Excimer Lasers," AIAA Journal **37**, 708–714 (1999).

[52] M. A. André, R. A. Burns, P. M. Danehy, S. R. Cadell, B. G. Woods, and P. M. Bardet, "Development of N_2O-MTV for low-speed flow and in-situ deployment to an integral effect test facility," Experiments in Fluids **59**, 14 (2018).

[53] F. K. Lu and D. E. Marren, *Advanced Hypersonic Test Facilities* (AIAA, 2002).

[54] H. G. Hornung, "Experimental Hypervelocity Flow Simulation, Needs, Achievements and Limitations," in *Proceedings of the First Pacific International Conference on Aerospace Science and Technology* (Taiwan, 1993).

[55] J. Belanger and H. G. Hornung, "Transverse Jet Mixing and Combustion Experiments in Hypervelocity Flows," Journal of Propulsion and Power **12**, 186–192 (1996).

[56] C. Y. Wen and H. G. Hornung, "Non-equilibrium dissociating flow over spheres," Journal of Fluid Mechanics **299**, 389–405 (1995).

[57] P. H. Adam and H. G. Hornung, "Enthalpy Effects on Hypervelocity Boundary-layer Transition: Ground Test and Flight Data," Journal of Spacecraft And Rockets **34**, 614–619 (1997).

[58] K. Fujii and H. G. Hornung, "Experimental Investigation of High-Enthalpy Effects on Attachment-Line Boundary-Layer Transition," AIAA Journal **41**, 1282–1291 (2003).

[59] N. J. Parziale, J. E. Shepherd, and H. G. Hornung, "Differential Interferometric Measurement of Instability in a Hypervelocity Boundary Layer," AIAA Journal **51**, 750–754 (2013).

[60] N. J. Parziale, J. E. Shepherd, and H. G. Hornung, "Free-stream density perturbations in a reflected-shock tunnel," Experiments in Fluids **55**, 1665 (2014).

[61] N. J. Parziale, J. E. Shepherd, and H. G. Hornung, "Observations of hypervelocity boundary-layer instability," Journal of Fluid Mechanics **781**, 87–112 (2015).

[62] P. D. Germain and H. G. Hornung, "Transition on a Slender Cone in Hypervelocity Flow," Experiments in Fluids **22**, 183–190 (1997).

[63] J. S. Jewell, *Boundary-layer transition on a slender cone in hypervelocity flow with real gas effects*, Ph.D. thesis, California Institute of Technology (2014).

[64] J. S. Jewell, N. J. Parziale, I. A. Leyva, and J. E. Shepherd, "Effects of Shock-Tube Cleanliness on Hypersonic Boundary Layer Transition at High Enthalpy," AIAA Journal **55**, 332–338 (2017).

[65] M. Havermann, J. Haertig, C. Rey, and A. George, "PIV Measurements in Shock Tunnels and Shock Tubes," in *Particle Image Velocimetry: New Developments and Recent Applications* (Springer Berlin Heidelberg, Berlin, Heidelberg, 2008) pp. 429–443.

[66] J. L. Wagner, E. P. DeMauro, K. M. Casper, S. J. Beresh, K. P. Lynch, and B. O. Pruett, "Pulse-burst PIV of an impulsively started cylinder in a shock tube for Re > 105," Experiments in Fluids **59**, 106 (2018).

[67] A. A. Martinez, G. C. Orlicz, and K. P. Prestridge, "A new experiment to measure shocked particle drag using multi-pulse particle image velocimetry and particle tracking," Experiments in Fluids **56**, 1854 (2015).

[68] A. N. Perkins, M. Ramsey, and R. W. Pitz, "Investigation of a Bow Shock in a Shock Tube Flow Facility Using Hydroxyl Tagging Velocimetry (HTV)," in *49th AIAA Aerospace Sciences Meeting including the New Horizons Forum and Aerospace Exposition, Aerospace Sciences Meetings* (AIAA-2011-1092, Orlando, Fl, USA, 2011).

[69] J. L. Mills, C. I. Sukenik, and R. J. Balla, "Hypersonic Wake Diagnostics Using Laser Induced Fluorescence Techniques," in *Proceedings of 42nd AIAA Plasmadynamics and Lasers Conference* (AIAA 2011-3459, Honolulu, Hawaii, 2011).

[70] R. J. Balla and J. L. Everhart, "Rayleigh Scattering Density Measurements, Cluster Theory, and Nucleation Calculations at Mach 10," AIAA Journal **50**, 698–707 (2012).

[71] N. J. Parziale, M. S. Smith, and E. C. Marineau, "Krypton tagging velocimetry of an underexpanded jet," Applied Optics **54**, 5094–5101 (2015).

[72] D. Zahradka, N. J. Parziale, M. S. Smith, and E. C. Marineau, "Krypton tagging velocimetry in a turbulent mach 2.7 boundary layer," Experiments in Fluids **57**, 62 (2016).

[73] M. A. Mustafa, N. J. Parziale, M. S. Smith, and E. C. Marineau, "Amplification and structure of streamwise-velocity fluctuations in compression-corner shock-wave/turbulent boundary-layer interactions," Journal of Fluid Mechanics **863**, 1091–1122 (2019).

[74] M. A. Mustafa, N. J. Parziale, M. S. Smith, and E. C. Marineau, "Nonintrusive Freestream Velocity Measurement in a Large-Scale Hypersonic Wind Tunnel," AIAA Journal **55**, 3611–3616 (2017).

[75] M. A. Mustafa and N. J. Parziale, "Simplified read schemes for krypton tagging velocimetry in N_2 and air," Optics Letters **43**, 2909–2912 (2018).

[76] O. Echt, M. C. Cook, and A. W. Castleman, "Krypton dimers: Resonance-enhanced mpi via gerade states in the region of atomic $4p^55p$ configurations," The Journal of Chemical Physics **87**, 3276–3280 (1987).

[77] M. D. Perry and O. L. Landen, "Resonantly enhanced multiphoton ionization of krypton and xenon with intense ultraviolet laser radiation," Physical Review A **38**, 2815 (1988).

[78] J. C. Miller, "Two-photon resonant multiphoton ionization and stimulated emission in krypton and xenon," Physical Review A **40**, 6969–6976 (1989).

[79] S. J. Bajic, R. N. Compton, X. Tang, and P. Lambropoulos, "Resonantly enhanced multiphoton-ionization photoelectron spectroscopy of krypton and xenon: Experiment and theory," Physical Review A **44**, 2102 (1991).

[80] F. Brandi, W. Hogervorst, and W. Ubachs, "High-resolution vacuum-ultraviolet and ultraviolet photoionization spectroscopy of krypton," Journal of Physics B: Atomic, Molecular and Optical Physics **35**, 1071 (2002).

[81] Y. Shiu and M. A. Biondi, "Dissociative recombination in krypton: Dependence of the total rate coefficient and excited-state production on electron temperature," Physical Review Applied **16**, 1817–1820 (1977).

[82] M. A. Dakka, G. Tsiminis, R. D. Glover, C. Perrella, J. Moffatt, N. A. Spooner, R. T. Sang, P. S. Light, and A. N. Luiten, "Laser-based metastable krypton generation," Phys. Rev. Lett. **121**, 093201 (2018).

[83] A. G. Hsu, V. Narayanaswamy, N. T. Clemens, and J. H. Frank, "Mixture fraction imaging in turbulent non-premixed flames with two-photon LIF of krypton," Proceedings of the Combustion Institute **33**, 759–766 (2011).

[84] A. C. Eckbreth, *Laser Diagnostics for Combustion Temperature and Species*, 2nd ed. (Gordon and Breach Publications, 1996).

[85] P. Lambropoulos, "Topics on Multiphoton Processes in Atoms," Advances in Atomic and Molecular Physics **12**, 87–164 (1976).

[86] N. M. Khambatta, J. A. Oertel, R. Silk, L. J. Radziemski, and J. M. Mack, "Absolute excited state and ion densities from two-and three-photon processes in some 6p levels of atomic krypton," Journal of Applied Physics **64**, 4809–4814 (1988).

[87] N. M. Khambatta, L. J. Radziemski, and S. N. Dixit, "Upper bound for a three-photon excitation cross section in atomic argon in the ultraviolet regime," Physical Review A **39**, 3842–3845 (1989).

[88] D. R. Richardson, N. Jiang, H. U. Stauffer, S. P. Kearney, S. Roy, and J. R. Gord, "Mixture-fraction imaging at 1 kHz using femtosecond laser-induced fluorescence of krypton," Optics Letters **42**, 3498–3501 (2017).

[89] J. Bokor, J. Y. Zavelovich, and C. K. Rhodes, "Multiphoton ultraviolet spectroscopy of some 6*p* levels in krypton," Physical Review A **21**, 1453–1459 (1980).

[90] M. N. Slipchenko, J. D. Miller, S. Roy, J. R. Gord, S. A. Danczyk, and T. R. Meyer, "Quasi-continuous burst-mode laser for high-speed planar imaging," Optics Letters **37**, 1346–1348 (2012).

[91] D. G. Goodwin, "An Open-Source, Extensible Software Suite for CVD Process Simulation," in *Proceedings of CVD XVI and EuroCVD Fourteen, M Allendorf, F Maury, and F Teyssandier (Eds.)* (2003) pp. 155–162.

[92] S. Browne, J. Ziegler, and J. E. Shepherd, *Numerical Solution Methods for Shock and Detonation Jump Conditions*, GALCIT - FM2006-006 (2006).

[93] F. White, *Viscous Fluid Flow*, 3rd ed. (McGraw-Hill, 2006).

[94] J. J. Kuehl, "Thermoacoustic interpretation of second-mode instability," AIAA Journal **56**, 3585–3592 (2018).

[95] T. O'Haver, *A Pragmatic Introduction to Signal Processing* (University of Maryland at College Park, 1997).

[96] R. B. Hill and J. C. Klewicki, "Data reduction methods for flow tagging velocity measurements," Experiments in Fluids **20**, 142–152 (1996).